Journal of the Meteorological Society of Japan (2026) 104:39
https://doi.org/10.1007/s44394-026-00041-4

ARTICLE

Applicability of a modified weather research and forecasting (WRF) model to heavy rainfall information

Mikio Nakanishi[1] · **Youko Yoshizumi**[1]

Received: 31 May 2026 / Accepted: 14 October 2026
© The Author(s) 2026

Abstract
The Japan Meteorological Agency (JMA) issues "Forecast Information on Linear Rainbands" (FILR; translated by the authors) approximately half a day before the expected formation of linear rainbands. A linear rainband is identified according to a set of operational criteria. A modified Weather Research and Forecasting (WRF) model was applied to sixteen heavy rainfall events associated with erroneous FILR decisions. Ten of these events had no FILR issued but subsequently experienced linear rainbands (missed issuance). Model results were compared with radar/rain-gauge analyzed precipitation data, with a primary focus on maximum rainfall, one of the criteria. The model reasonably simulated the occurrence of heavy rainfall in eight of the ten events and the rainfall intensity in six of those eight events. Conversely, six of the sixteen events had FILRs issued but ultimately experienced no linear rainbands (false alarm). In five of these events, the model reasonably reproduced the observed rainfall that did not satisfy the linear-rainband criteria. These results suggest that, despite several remaining challenges, the modified WRF model has the potential to complement JMA FILR decisions and contribute to reducing both missed issuances and false alarms.

Keywords Heavy rainfall · Linear rainband · Mass-flux scheme · Turbulent buoyancy production · Weather research and forecasting model

1 Introduction

Since 2022, we have been modifying version 4.3.3 of the Weather Research and Forecasting (WRF) model (Skamarock et al. 2019) to improve our weather forecasting services. Nakanishi (2025) demonstrated that the modified WRF model improves the reproduction of a linear rainband event. This study evaluates the performance of the modified WRF model for a larger number of heavy rainfall events, including linear rainbands, and its applicability to heavy rainfall information.

The Japan Meteorological Agency (JMA) uses a set of criteria to identify linear rainbands and issues "Occurrence Information on Linear Rainbands" (OILR; translated by the authors) immediately before their formation. According to JMA (2026a), the criteria include the area, shape, and maximum rainfall of a rainband, as well as the degree of danger (Kikikuru; Ota and Igarashi 2026). The objective of this study is to forecast heavy rainfall rather than to reproduce all the criteria used to identify linear rainbands. Therefore, the evaluation focuses primarily on the maximum rainfall criterion of 150 mm in 3 h and secondarily on the area criterion of 500 km^2 with rainfall exceeding 100 mm in 3 h. The shape criterion, which requires a major-to-minor axis ratio of 2.5 or greater for a rainband, is excluded because heavy rainfall can occur even in a circular rainband. Furthermore, Kikikuru cannot be estimated from the WRF model output.

We briefly describe the modification of the WRF model. An earlier version of the WRF model with a horizontal resolution of 5 km did not satisfactorily simulate several heavy rainfall events. To investigate possible limitations of the subgrid-scale parameterizations, Nakanishi (2024) compared simulations with horizontal resolutions of 5 km and 1 km, using the same topographic resolution for both. He suggested that improving the parameterization of turbulent transport processes near the level of free convection could lead to more accurate predictions of the timing and location of rainband formation.

✉ Mikio Nakanishi
nakanishi.mikio@jwa.or.jp

[1] Japan Weather Association, 3-1-1 Higashi-ikebukuro, Toshima 170- 6055, Tokyo, Japan

Published online: 04 November 2026

The 5-km simulation employed a mass-flux scheme to parameterize convection, including shallow cumulus convection (Sušelj et al. 2013). However, Nakanishi (2025) noted that the mass-flux contribution was not explicitly included in the turbulent kinetic energy (TKE) equation and consequently modified the buoyancy production term. This modified model reasonably reproduced a rainband that the earlier version had failed to simulate. Since then, the modified version has undergone further refinements to subgrid-scale parameterizations to improve the simulation of various phenomena, such as heavy snowfall associated with winter cold-air outbreaks. In this paper, we apply the latest version of the modified WRF model to sixteen heavy rainfall events.

As reviewed in detail by Kato (2020), numerous numerical studies of linear rainbands have been conducted. However, most have been case studies focusing on the formation and maintenance mechanisms of linear rainbands (e.g., Kato and Goda 2001; Kawano and Kawamura 2020; Tochimoto et al. 2022; Ono and Ito 2024), the effects of model configuration and planetary boundary layer schemes (e.g., Oizumi et al. 2018), and data assimilation (e.g., Kawabata et al. 2011; Kato et al. 2024). In March 2026, the JMA began operational use of a regional model with a horizontal resolution of 1 km (JMA 2026b). Although the JMA model represents topographic effects more accurately, it still relies on subgrid-scale parameterizations. Owing to limitations in computational resources, we retain a horizontal resolution of 5 km. Therefore, favorable performance of the modified WRF model may indicate improvements that are independent of detailed topographic representation. Such improvements may also contribute to the development of subgrid-scale parameterizations for 1-km resolution models.

Section 2 describes the computational domain, model configuration, and numerical settings. Section 3 presents refinements to the mass-flux scheme and related parameterizations since Nakanishi (2025). Section 4 evaluates the modified WRF model using heavy rainfall events. Section 5 discusses the remaining challenges of the model.

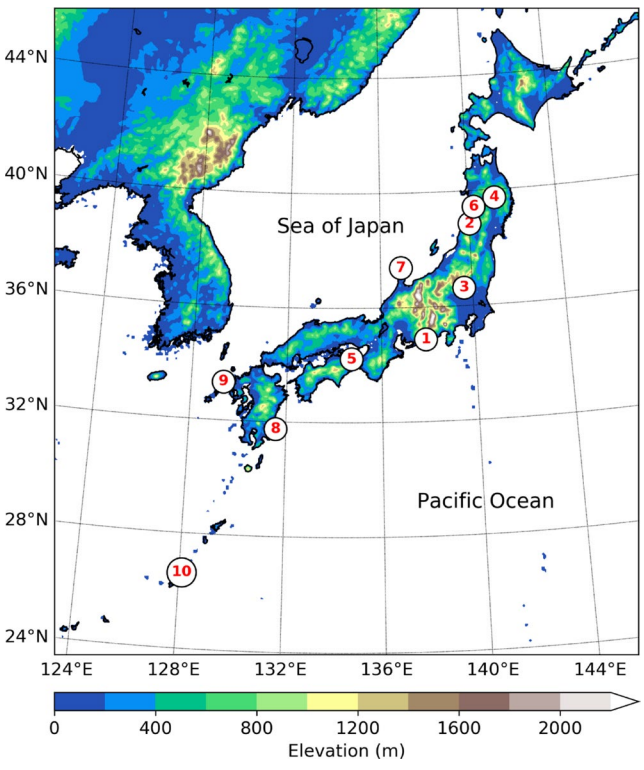


Fig. 1 Model domain. Shading indicates topography. Numbers denote the locations of observed linear rainbands and correspond to the case numbers listed in Table 1

2 Model setup

The modified WRF model was applied to the region surrounding Japan (Fig. 1). This domain consists of 455 × 503 horizontal grid points with a resolution of 5 km and 45 stretched vertical levels with the model top at 50 hPa. The physics parameterizations are identical to those used by Nakanishi (2025):

- Mellor–Yamada–Nakanishi–Niino (MYNN) level 2.5 scheme (bl_pbl_physics = 5),
- Mass-flux scheme (bl_mynn_edmf = 1),
- Partial condensation scheme (bl_mynn_cloudpdf = 0),
- Surface layer scheme (sf_sfclay_physics = 5),
- Noah multi-parameterization scheme (sf_surface_physics = 4),
- Aerosol-aware Thompson–Eidhammer scheme (mp_physics = 28), and.
- Rapid Radiative Transfer Model for GCMs (ra_sw(lw)_physics = 4),

where the option numbers are given in parentheses. The Noah multi-parameterization scheme was modified by Nakanishi (2023).

The JMA issues "Forecast Information on Linear Rainbands" (FILR; translated by the authors) approximately half a day before the expected formation of linear rainbands. The modified WRF model simulated sixteen heavy rainfall events associated with erroneous FILR decisions (JMA 2026a). Ten of these events (Table 1) had no FILR issued but subsequently experienced linear rainbands (missed issuance), resulting in the issuance of OILRs. Conversely, the remaining six events (Table 2) had FILRs issued but ultimately experienced no linear rainbands (false alarm), resulting in no OILR issuance.

Each simulation was initialized approximately 20 h before the observed peak rainfall time and integrated for 27 h. This 20-h lead time was empirically determined by considering both model spin-up from the initial conditions and the

Table 1 Ten missed-issuance cases in 2024 (JMA 2026a). The location of each rainband is indicated by the corresponding case number in Fig. 1

Case	Prefecture	Peak rainfall mm/3 h	Peak time month/day hour	Initial time month/day hour	Forecast time month/day hour
1	Shizuoka	164	06/28 11	06/27 15	06/28 12
2	Yamagata	151	07/25 23	07/25 03	07/26 00
3	Tochigi	240	08/26 02	08/25 03	08/26 02
4	Iwate	208	08/27 21	08/26 21	08/27 20
5	Hyogo	212	08/29 19	08/28 21	08/29 19
6	Akita	142	09/20 05	09/19 09	09/20 06
7	Ishikawa	223	09/21 11	09/20 15	09/21 10
8	Miyazaki	290	10/22 17	10/21 21	10/22 18
9	Nagasaki	183	11/02 02	11/01 03	11/02 03
10	Okinawa	345	11/09 03	11/08 03	11/09 03

Times are given in Japan Standard Time (JST = UTC + 9). Peak and Forecast times denote the times at which the maximum 3-h accumulated rainfall occurs in the radar/rain-gauge analyzed (RRA) precipitation data and the modified WRF model, respectively. Peak rainfall denotes the corresponding maximum 3-h accumulated rainfall in the RRA data

Table 2 Same as Table 1, but for six false-alarm cases in 2024 (JMA 2026a). No linear rainbands were identified in these cases

Case	Region	Peak rainfall mm/3 h	Peak time month/day hour	Initial time month/day hour	Forecast time month/day hour
A	Tokai	114	05/28 20	05/27 21	05/28 22
B	Shikoku	136	06/18 07	06/17 09	06/18 08
C	Tohoku	99	08/12 02	08/11 09	08/12 02
D	Kanto	80	08/16 18	08/15 21	08/16 18
E	Tohoku	111	08/17 06	08/16 09	08/17 07
F	Tokai	134	08/27 08	08/26 15	08/27 08

For Case A only, the peak and forecast rainfall times differ by two hours

gradual degradation of forecast accuracy with increasing lead time. The initial and lateral boundary conditions were provided by real-time forecasts from the European Centre for Medium-Range Weather Forecasts (ECMWF) with temporal and spatial resolutions of 3 h and 0.25°, respectively (ECMWF 2026a). Sea surface temperatures were prescribed from the daily High-resolution Merged Satellite and In-situ Data SST (HIMSST) dataset with a spatial resolution of 0.1° (JMA 2026c).

3 Model refinements

The modified WRF model is identical to that described by Nakanishi (2025), except for minor refinements to the mass-flux scheme and related parameterizations.

3.1 Mass-flux scheme and buoyancy production

Siebesma and Cuijpers (1995) derived a mass-flux formulation by decomposing the vertical turbulent flux $\overline{w'\phi'}$ of any variable ϕ into three contributions, where w is the vertical velocity, the overbar denotes the ensemble mean, and the prime denotes the deviation from the ensemble mean. Olson et al. (2019) incorporated the mass-flux scheme into the MYNN scheme of the WRF model. Assuming that the fractional area occupied by updrafts is much smaller than unity, $\overline{w'\phi'}$ can be expressed as the sum of eddy-diffusivity and mass-flux contributions:

$$\overline{w'\phi'} = -K\frac{\partial\overline{\phi}}{\partial z} + \sum_{i=1}^{n} a_{ui}\left(w_{ui}-\overline{w}\right)\left(\phi_{ui}-\overline{\phi}\right), \tag{1}$$

where K is the eddy-diffusivity coefficient obtained from the MYNN scheme, n is the number of updraft plumes, a_{ui} is the area fraction of plume i, w_{ui} is the vertical velocity of plume i, and ϕ_{ui} denotes ϕ for plume i. We replace $\sum_{i=1}^{n} a_{ui}$, which is a function of surface heat flux in Olson et al. (2019), with a constant value of 0.05 following Köhler et al. (2011), except when $a_{ui}=0$ under stable conditions with negative surface heat fluxes. In addition, we approximate $w_{ui}-\overline{w}\approx w_{ui}$, following Olson et al. (2019).

The virtual potential temperature flux $\overline{w'\theta_v'}$, which contributes to TKE production, is given by

$$\overline{w'\theta_v'} = A\,\overline{w'\theta_l'} + B\,\overline{w'q_w'} + C\,\overline{w'q_l'}, \tag{2}$$

where θ_v is the virtual potential temperature, θ_l is the liquid water potential temperature, q_w is the total water content, and q_l is the liquid water content. The coefficients A, B, and C are

$$A = 1 + 0.61\overline{q}_w - 1.61\overline{q}_l, \tag{3a}$$

$$B = 0.61\overline{\theta}, \tag{3b}$$

$$C = A\frac{L_v}{c_p}\frac{\overline{\theta}}{\overline{T}} - 1.61\overline{\theta}, \tag{3c}$$

where T is the absolute temperature, c_p is the specific heat of dry air at constant pressure, and L_v is the latent heat of vaporization. Substituting Eq. (1) into Eq. (2) yields

$$\overline{w'\theta_v'} = \overline{w'\theta_v'}_{\mathrm{PCS}} + \sum_{i=1}^{n} a_{ui}w_{ui}\left(A\Delta_i\theta_l + B\Delta_i q_w + C\Delta_i q_l\right), \tag{4}$$

where $\overline{w'\theta_v'}_{\mathrm{PCS}}$ is obtained from the partial condensation scheme (e.g., Nakanishi and Niino 2009) and $\Delta_i\phi = \phi_{ui} - \overline{\phi}$.

Equation (4) was described in Text S2 of Nakanishi (2025). As an alternative, he also proposed a formulation that blends the effects of plume and non-plume regions. Although this formulation can be applied to models without a mass-flux scheme, its performance depends strongly on the choice of the probability density function in plume regions. In contrast, Eq. (4) is a straightforward formulation within the mass-flux framework that explicitly accounts for the effects of plume regions. The sign of the mass-flux term, i.e., the second term on the right-hand side of Eq. (4), depends on the value of $\Delta_i\phi$. A positive mass-flux term enhances TKE production, whereas a negative term reduces it. Consequently, increased TKE can help air parcels in the lower layer rise above the level of free convection.

3.2 Plume model

3.2.1 Equations

The plume model calculates ϕ_{ui} and w_{ui}. The equations for ϕ_{ui} and w_{ui} are given by

$$\frac{\partial \phi_{ui}}{\partial z} = -\epsilon_i \left(\phi_{ui} - \overline{\phi}\right), \tag{5}$$

$$\frac{1}{2}\frac{\partial w_{ui}^2}{\partial z} = -\alpha \epsilon_i w_{ui}^2 + \beta g \frac{\theta_{v,ui} - \overline{\theta}_v}{\overline{\theta}_v}, \tag{6}$$

where ϵ_i is the fractional entrainment rate and g is the acceleration due to gravity. We replace the coefficients $\alpha = 2$ and $\beta = 0.15$ used by Olson et al. (2019) with $\alpha = 1$ and $\beta = 1$ following Köhler et al. (2011) and Neggers (2015). Accordingly, ϵ_i is obtained from the empirical formulation of Neggers (2015):

$$\epsilon_i = 0.02\, d_i^{-0.35}, \tag{7}$$

where d_i is the diameter of plume i. As in Olson et al. (2019), we assume that $d_i = i \times 100$ m ($1 \le i \le n$) and that d_i remains constant with height, where n is 10 or less depending on the grid spacing and the depth of the mixed layer. Equations (5) and (6) are integrated from the lowest level to the level at which w_{ui} vanishes.

3.2.2 Lower boundary condition

The initialization of plumes at the lowest level z_1 within the surface layer is also modified following Köhler et al. (2011). $\phi_{ui}(z_1)$ and $w_{ui}(z_1)$ at z_1 are given by

$$\phi_{ui}(z_1) = \overline{\phi}(z_1) + c\frac{\overline{w'\phi'}_s}{\sigma_w}, \tag{8}$$

$$w_{ui}(z_1) = c\sigma_w, \tag{9}$$

where the subscript s denotes the surface layer. If z_1 is much smaller than the depth of the mixed layer, the standard deviation σ_w of vertical velocity is empirically obtained as

$$\sigma_w \approx 1.2\left(u_*^3 + 1.5k\frac{g}{\overline{\theta}_{v,s}}\overline{w'\theta'}_{vs} z_1\right)^{1/3}, \tag{10}$$

where u_* is the friction velocity and k is the von Kármán constant. Unlike Köhler et al. (2011), who set $c = 2.05$ corresponding to $\sum_{i=1}^{n} a_{ui} = 0.05$, we use

$$c = \min\left[2.05, \left(\frac{K\frac{\partial \overline{\theta}}{\partial z}\Big|_{z_1} + \overline{w'\theta'}_s}{\sum_{i=1}^{n} a_{ui}\overline{w'\theta'}_s}\right)^{1/2}\right]. \tag{11}$$

This upper limit ensures that the vertical heat flux at z_1, calculated from Eqs. (1), (8), and (9), remains smaller than $\overline{w'\theta'}_s$, thereby preventing unintended cooling of $\overline{\theta}$ at the lowest layer.

4 Results

We compared the horizontal distributions of simulated rainfall with radar/rain-gauge analyzed (RRA) precipitation data (Nagata 2011) on an hourly basis. The comparison was conducted at the time when the simulated 3-h accumulated rainfall reached its maximum within ±2 h of the observed peak rainfall time (see Tables 1 and 2). In addition, OILRs are issued using 3-h accumulated RRA precipitation data on a ten-minute basis. Therefore, the observed rainbands shown in Figs. 2, 3, 4 and 5 do not necessarily satisfy all the criteria defined by JMA (2026a). For reference, Figs. 2, 3, 4, 5, 6, 7 and 8 also show results from the WRF model using the original mass-flux scheme of Olson et al. (2019) (ORG), which does not include the second term on the right-hand side of Eq. (4). The unit of 3-h accumulated rainfall (mm per 3 h) is hereafter abbreviated as mm. The issues identified in this section are further discussed in Sect. 5.

4.1 Missed-issuance cases

Based on the characteristics of heavy rainfall events and the forecast performance, we classified the ten cases in Table 1 into four categories: daytime, coastal, nighttime, and forecast-failure cases.

4.1.1 Daytime cases

Figure 2 shows the horizontal distributions of 3-h accumulated rainfall from the RRA data, the modified WRF model, and the ORG model for Cases 1, 7, and 8. Surface winds from the

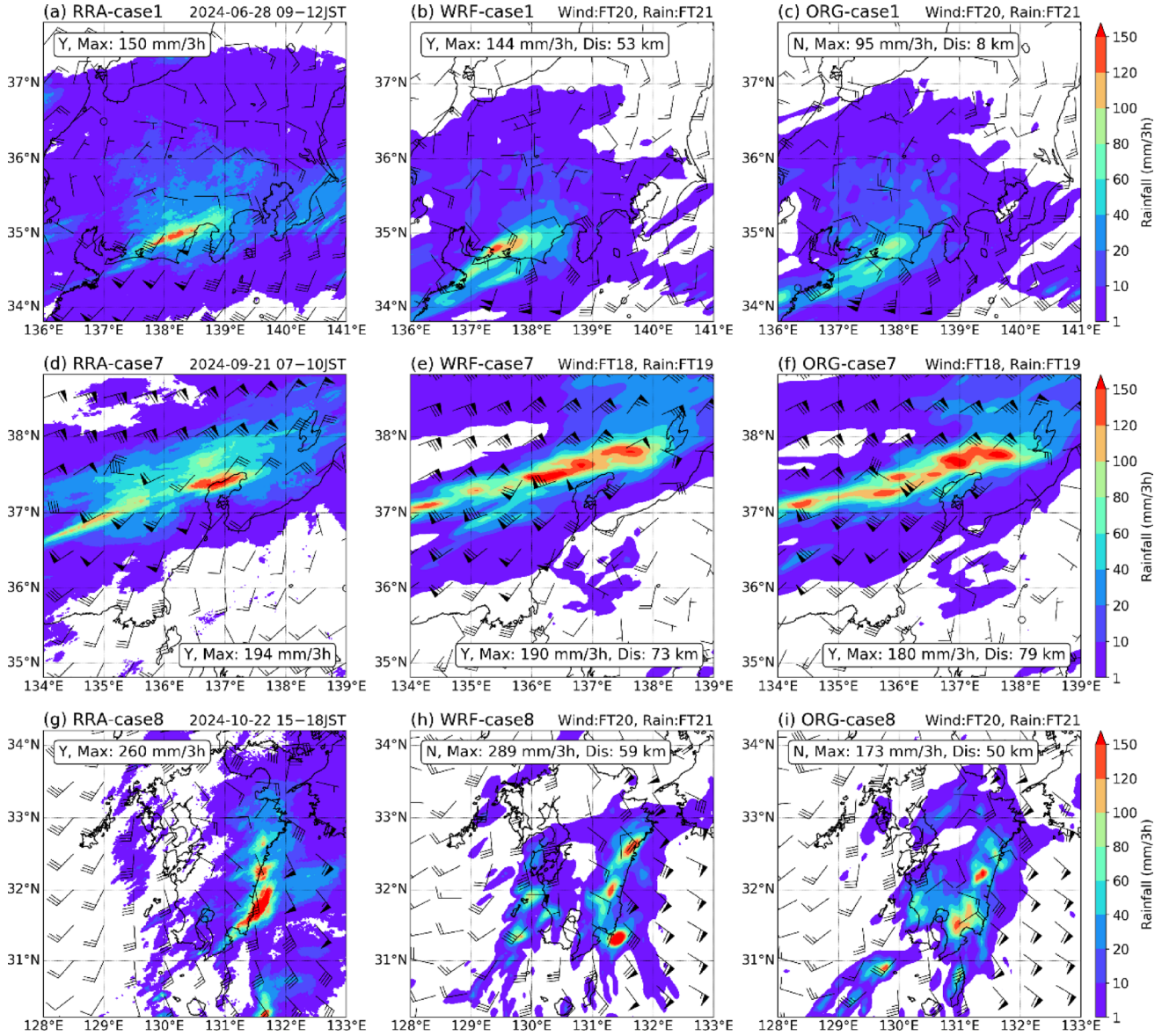


Fig. 2 Horizontal distributions of 3-h accumulated rainfall from (a, d, g) the RRA data, (b, e, h) the modified WRF model, and (c, f, i) the ORG model for Cases 1 (a–c), 7 (d–f), and 8 (g–i). The information box in the upper-left or lower-right portion of each panel shows the 500-km^2 area criterion (Y: satisfied, N: not satisfied), the maximum rainfall (Max), and the distance between the rainfall maxima in the RRA data and the modified WRF or ORG model (DIS). Barbs show surface winds at 10 m above ground level from (a, d, g) the ERA5 data, (b, e, h) the modified WRF model, and (c, f, i) the ORG model one hour before the end of the 3-h accumulation period. A flag, full barb, half barb, and circle denote wind speeds of 10, 2, 1, and <0.5 m s^{-1}, respectively

5th-generation ECMWF Reanalysis (ERA5) data (ECMWF 2026b) are used as a proxy for observed surface winds.

For Case 1, the RRA data (Fig. 2a) show a linear rainband with a maximum rainfall of 150 mm on a south-facing slope in the Tokai region (point 1 in Fig. 1). The ERA5 surface winds blow toward the slope from the southwest. The WRF model (Fig. 2b) reasonably reproduces the rainband and satisfies the criterion requiring an area of at least 500 km^2 with rainfall exceeding 100 mm (JMA 2026a). The maximum rainfall of 144 mm simulated by the WRF model is only slightly lower than the criterion requiring a maximum rainfall of 150 mm or more (JMA 2026a). In contrast, the distance between the rainfall maxima in the RRA data and the WRF model (DIS) is 53 km. This westward displacement of the simulated rainband is consistent with the WRF surface winds being more easterly than the ERA5 winds. The ORG model (Fig. 2c) satisfies neither the rainfall nor the area criterion.

For Case 7, an east-west-oriented stationary front is inferred from the convergence line of the ERA5 surface winds (Fig. 2d) and the distribution of simulated surface heat flux (Figs. S1d and S1e). The RRA data (Fig. 2d) show a linear rainband aligned with the front, with enhanced rainfall over the Noto

Peninsula (point 7 in Fig. 1). The WRF model (Fig. 2e) satisfies both the rainfall and area criteria; however, the simulated rainband is located north of the peninsula along the convergence line of the WRF surface winds and covers a larger area with rainfall exceeding 100 mm than the observed rainband. The ORG model (Fig. 2f) exhibits similar performance.

For Case 8, the RRA data (Fig. 2g) show three rainbands along the eastern coast of Kyushu, a large island in southwestern Japan. The southernmost rainband produced particularly heavy rainfall. The ERA5 surface winds blow toward the eastern coast from the southeast. The WRF model (Fig. 2h) also simulates three rainbands in similar locations. However, the southernmost simulated rainband is displaced southward with a DIS of 59 km. This displacement is consistent with the WRF surface winds being more easterly than the ERA5 winds. Although the compact spatial extent of the simulated rainband prevents it from satisfying the area criterion, its maximum rainfall satisfies the rainfall criterion. The ORG model (Fig. 2i) also satisfies the rainfall criterion but simulates the rainbands farther inland than observed, on the lee side of the eastern coast.

4.1.2 Coastal cases

Figure 3 is the same as Fig. 2, but for Cases 2, 6, and 9. Based on weather charts (e.g., JWA 2026), these cases were associated with frontal systems. The simulated surface heat

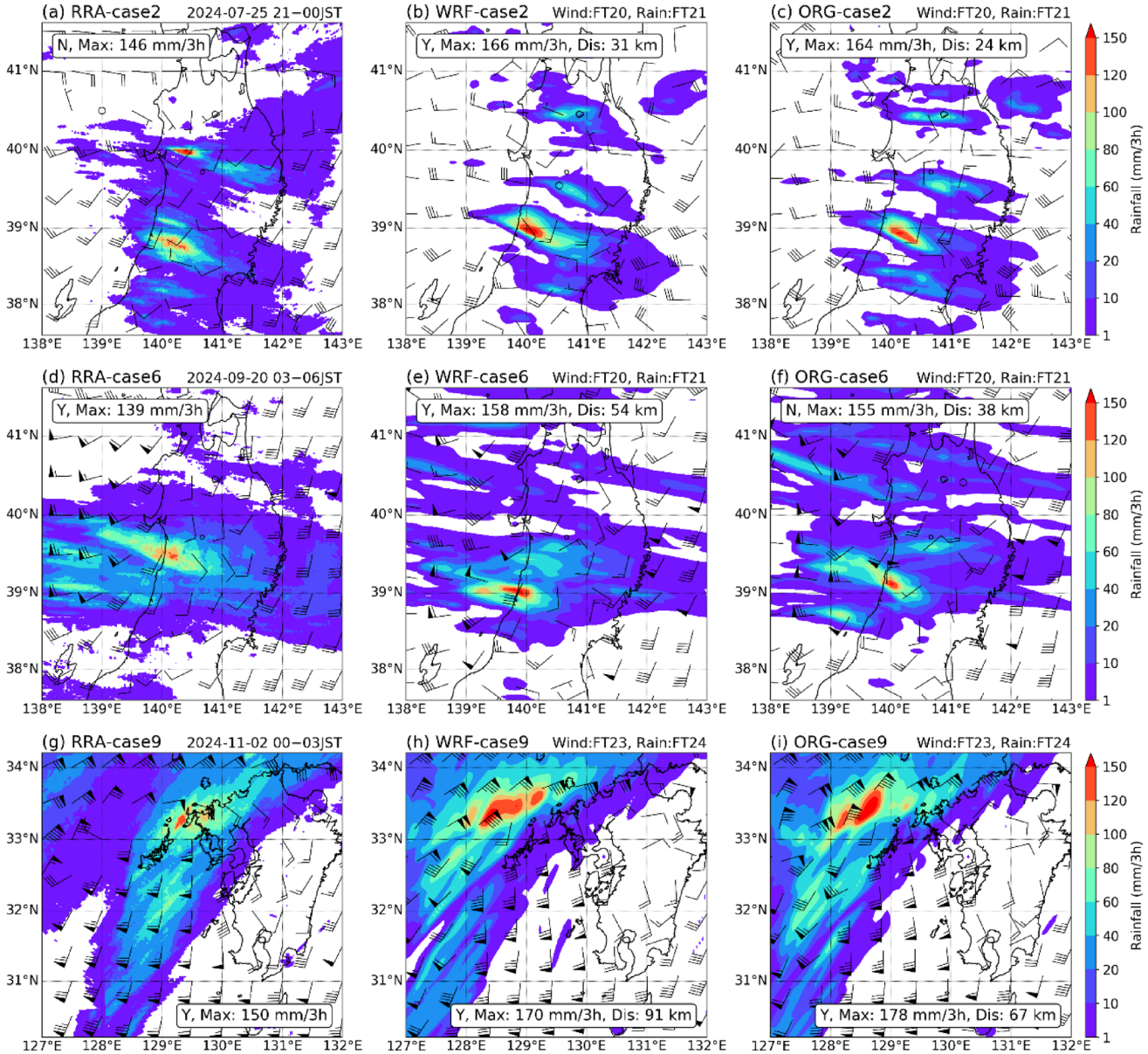


Fig. 3 Same as Fig. 2, but for Cases 2 (a–c), 6 (d–f), and 9 (g–i). The rainband near 40°N, 140°E in (a) is excluded from the linear-rainband analysis (see text)

flux (Fig. S2) and surface wind fields (especially Fig. 3h and i) suggest that both the WRF and ORG models simulate rainbands forming on the positive side of the zero-flux line and north of the frontal boundary.

For Case 2, the RRA data (Fig. 3a) show two rainbands: a northern rainband near 40°N, 140°E and a southern rainband near 39°N, 140°E. The northern rainband produced a maximum rainfall of 184 mm but did not satisfy the area criterion. The maximum rainfall of 146 mm shown in Fig. 3a was recorded in the southern rainband. Although the southern rainband narrowly missed both the rainfall and area criteria at this time, an OILR was issued for this event. Both the WRF and ORG models (Fig. 3b and c) reasonably reproduce the southern rainband and satisfy both the rainfall and area criteria. Conversely, both models fail to reproduce the northern rainband. Mount Moriyoshi is located at 39.98°N, 140.55°E, near the rainband. Its elevation is 1,454 m, whereas the elevation of the 5-km grid cell containing the mountain is about 800 m. A finer grid spacing may be required to adequately resolve the terrain around Mount Moriyoshi and thereby reproduce the northern rainband.

For Case 6, the RRA data (Fig. 3d) show a rainband near 39.5°N, 140°E, with a maximum rainfall of 139 mm at this time. Although the WRF model simulates rainfall exceeding 60 mm in the same region, another rainband near Mount Chokai (39.10°N, 140.05°E) produces a maximum rainfall of 158 mm (Fig. 3e). Over the Sea of Japan west of the mountain, the WRF surface winds (Fig. 3e) are more northerly than the ERA5 winds (Fig. 3d). This difference in wind direction, together with the presence of the mountain, may contribute to the displacement of the simulated rainband. The ORG model (Fig. 3f) does not satisfy the area criterion.

For Case 9, the RRA data (Fig. 3g) show a rainband near the coast of northwestern Kyushu, while the WRF model (Fig. 3h) simulates a rainband over the sea west of the observed rainband. The DIS is 91 km, which is the largest among the missed-issuance cases excluding the forecast-failure cases. As in Case 7 (Fig. 2d and e), the displacement of the simulated rainband illustrates the difficulty of accurately predicting the location of frontal wind convergence. However, the presence of clearly distinguishable fronts (see Figs. S1d, S1e, S2g, and S2h) appears to facilitate rainband prediction. Both the WRF and ORG models (Fig. 3h and i) simulate the rainband and satisfy both the rainfall and area criteria.

4.1.3 Nighttime cases

Figure 4 is the same as Fig. 2, but for Cases 3 and 4. Based on the weather charts for these cases (e.g., JWA 2026), although a typhoon was moving northward over the ocean

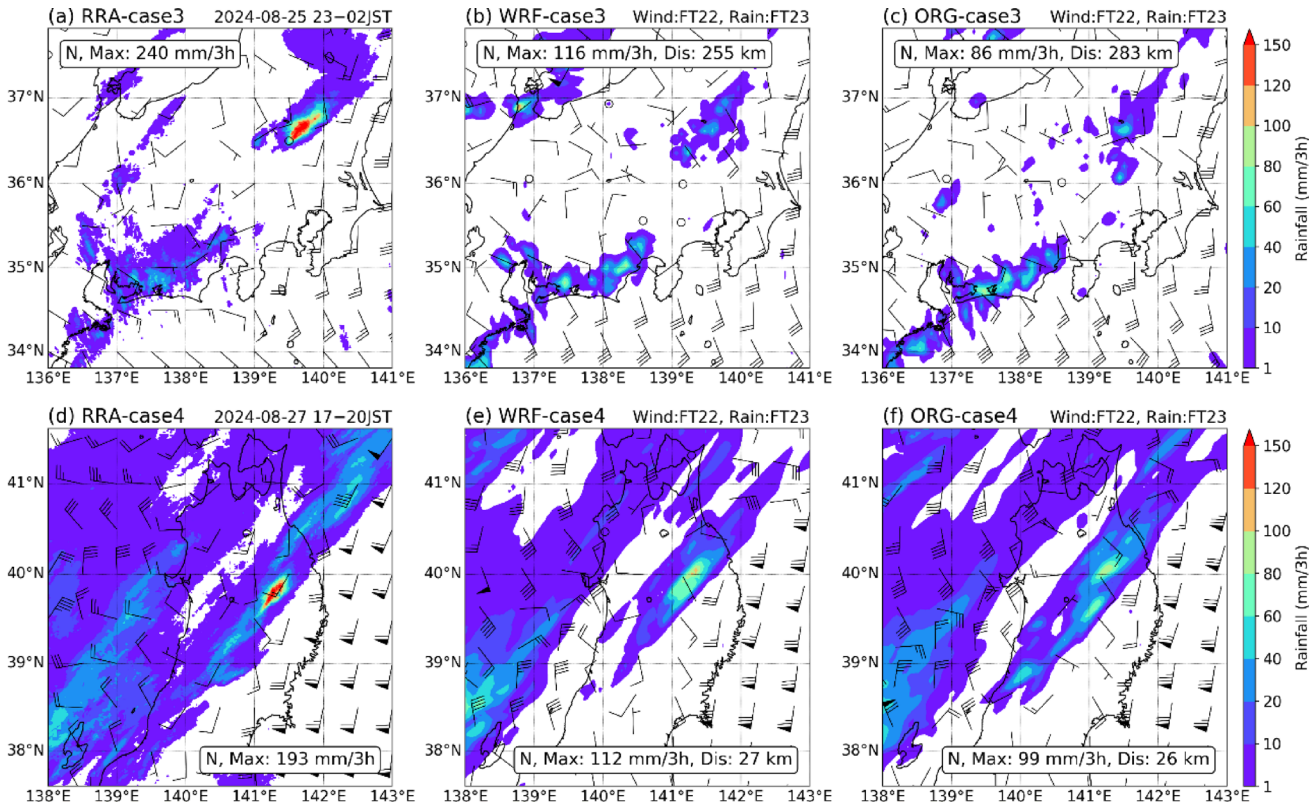


Fig. 4 Same as Fig. 2, but for Cases 3 (a–c) and 4 (d–f)

south of Kyushu, Japan was located on the western periphery of the Pacific high-pressure system.

For Case 3, the RRA data (Fig. 4a) show a rainband on an inland southeast-facing slope. The ERA5 surface winds are southerly, suggesting that the rainband developed primarily through upslope lifting. The WRF model (Fig. 4b) simulates rainfall exceeding 40 mm near the observed rainfall but satisfies neither the rainfall nor the area criterion. A simulated maximum rainfall of 116 mm occurs in the Noto Peninsula, resulting in a DIS of 255 km. The ORG model (Fig. 4c) also exhibits similar characteristics. As in Case 1 (Fig. 2a and b), rainfall exceeding 40 mm occurs on the south-facing slope in the Tokai region, suggesting that this region may be susceptible to heavy rainfall under warm, moist southerly flow.

For Case 4, the RRA data (Fig. 4d) show a rainband with a maximum rainfall of 193 mm near 40°N, 141°E. The ERA5 surface winds blow toward the rainband from the south. This rainband appears to have formed under the influence of topography in the northern part of a basin extending from north to south. The WRF model (Fig. 4e) simulates the rainband with a lower maximum rainfall of 112 mm. In addition, the simulated rainband is displaced to the lee side of the observed rainband. However, the DIS is only 27 km, the smallest among the missed-issuance cases. The ORG model (Fig. 4f) also exhibits similar characteristics. Cases 3 and 4 suggest that the underestimation of rainfall and the leeward displacement of simulated rainbands may result from the ineffectiveness of the mass-flux scheme under nocturnal stable conditions (see Sect. 3.1).

4.1.4 Forecast-failure cases

Figure 5 is the same as Fig. 2, but for Cases 5 and 10. In these cases, the WRF model failed to reproduce the observed rainbands.

For Case 5, a typhoon made landfall in Kyushu around 08 JST on 29 August (e.g., JWA 2026). The RRA data (Fig. 5a) show a linear rainband in northeastern Shikoku, the fourth-largest island in Japan. However, both the WRF and ORG models (Fig. 5b and c) simulate a weaker rainband, located slightly west of the observed rainband, that does not satisfy the rainfall criterion. Instead, the WRF model (Fig. 5b) generates a spurious rainband near 34.5°N, 136.5°E.

For Case 10, Okinawa Island, located south of Kyushu, was situated on the southern periphery of a high-pressure system and within a weak pressure trough (e.g., JWA 2026). The RRA data (Fig. 5d) show a linear rainband northeast of Okinawa Island, together with a rainfall pattern resembling that around a low-pressure system. However, neither the WRF nor ORG model (Fig. 5e and f) reproduces the

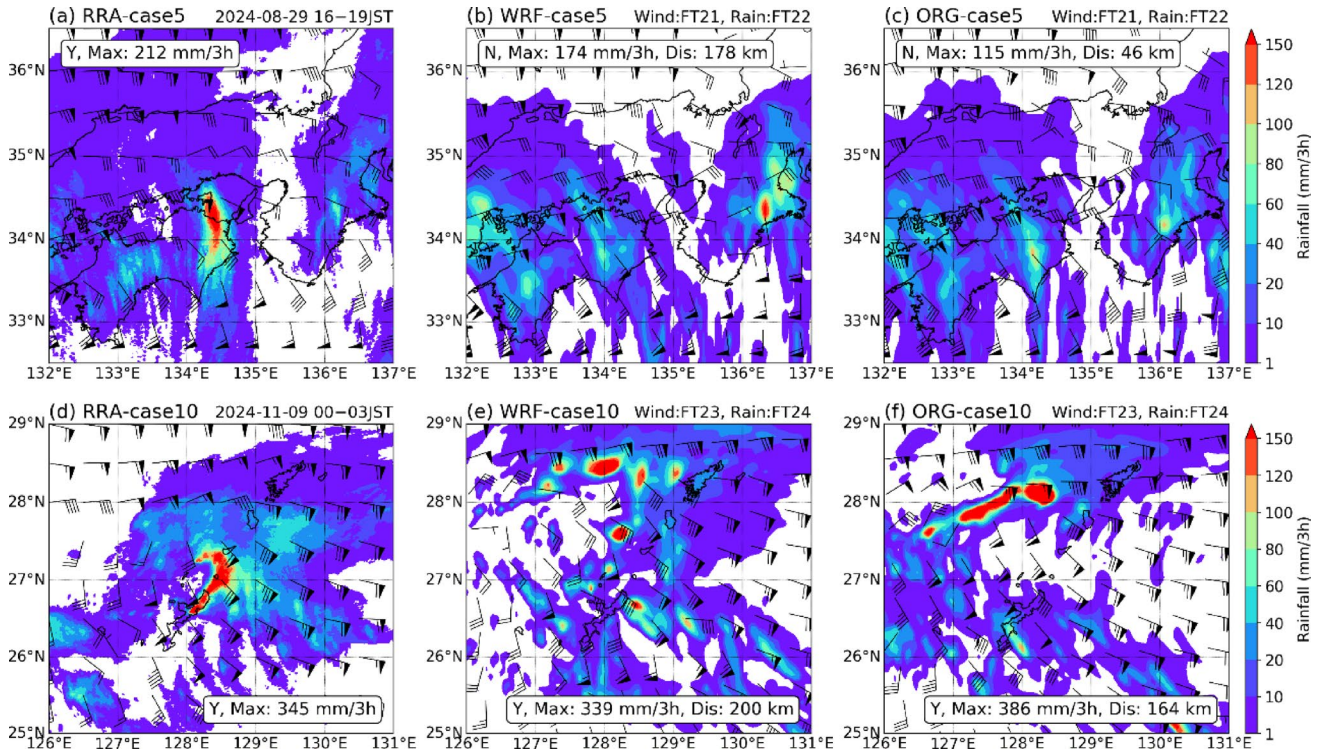


Fig. 5 Same as Fig. 2, but for Cases 5 (a–c) and 10 (d–f)

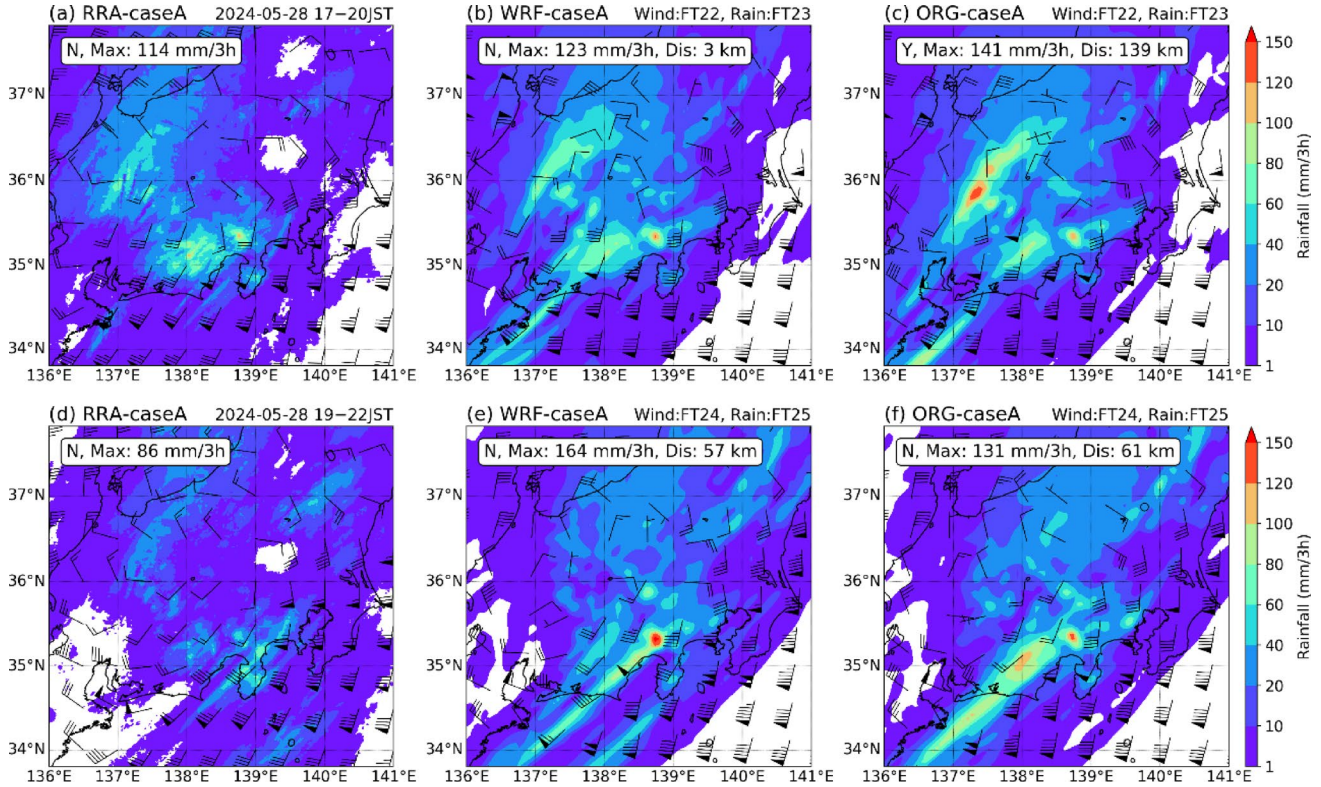


Fig. 6 Same as Fig. 2, but for Case A at 20 JST (a–c) and 22 JST (d–f) on 28 May

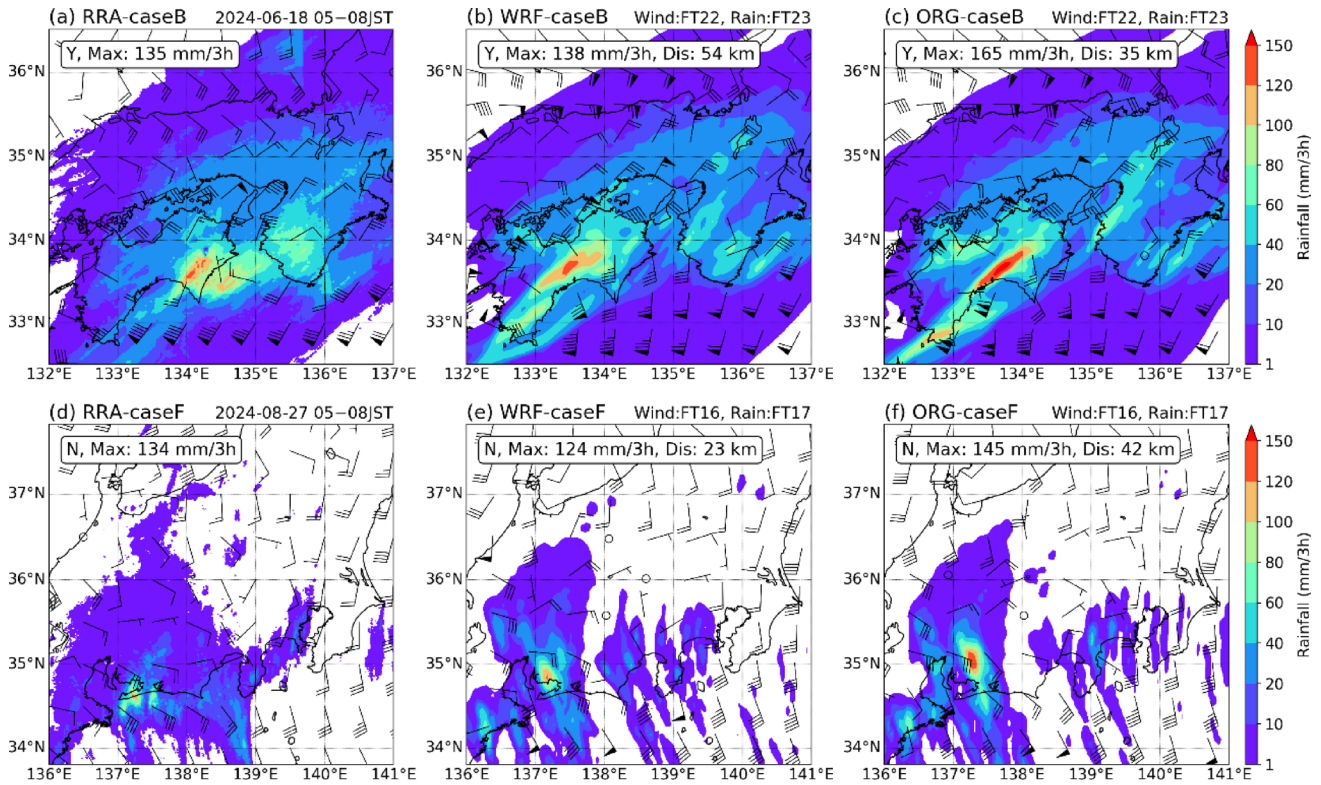


Fig. 7 Same as Fig. 2, but for Cases B (a–c) and F (d–f)

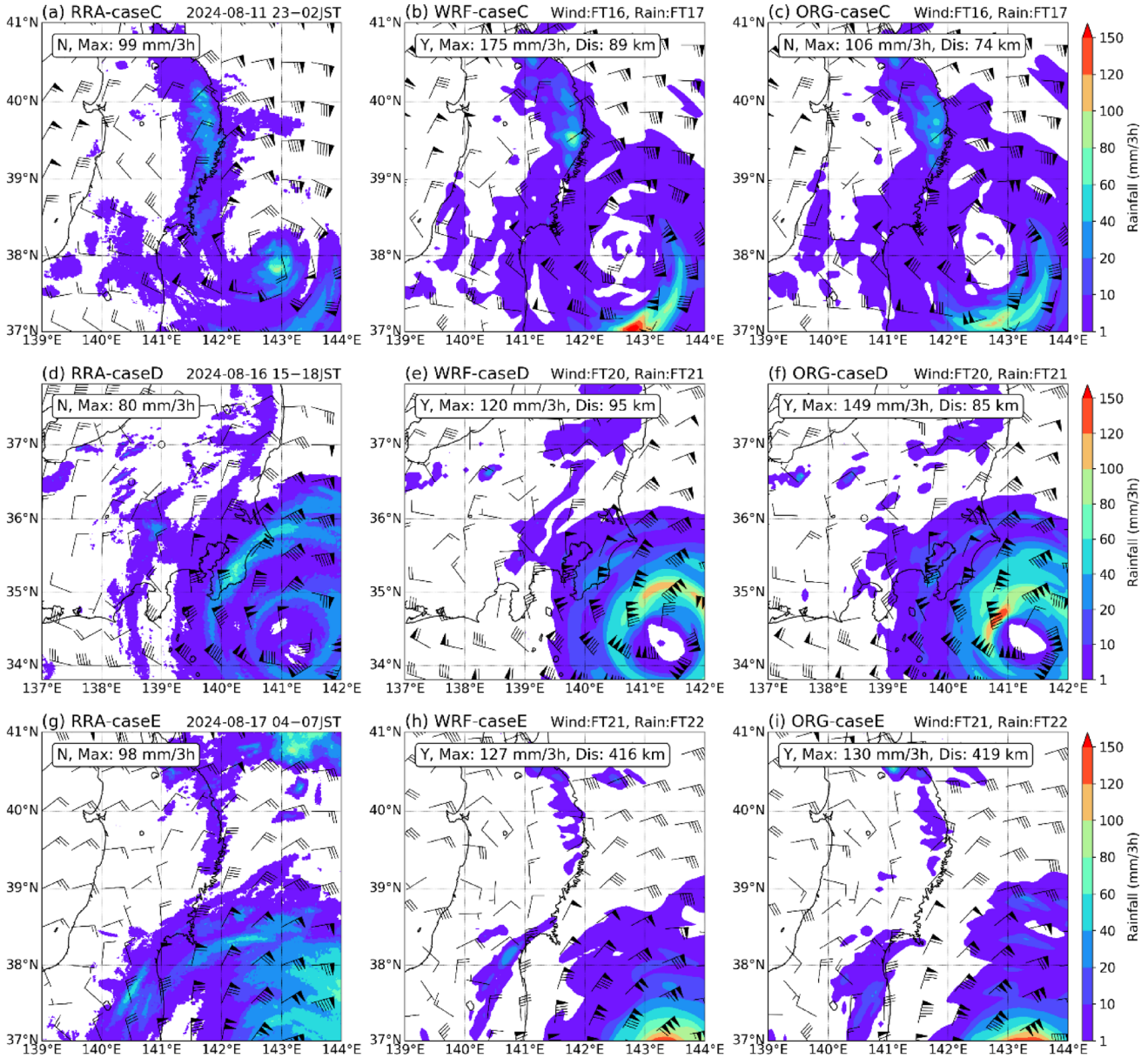


Fig. 8 Same as Fig. 2, but for Cases C (a–c), D (d–f), and E (g–i)

overall rainfall pattern or the rainband. In particular, the ORG model (Fig. 5f) fails to reproduce the observed rainfall area northeast of Okinawa Island.

4.2 False-alarm cases

For convenience, we divided the six cases in Table 2 into three groups. In this study, the primary goal for false-alarm cases is to keep the simulated maximum rainfall below the rainfall criterion of 150 mm (JMA 2026a).

4.2.1 Case A

Figure 6 is the same as Fig. 2, but for Case A. For this case, the peak rainfall times in the RRA data and the WRF model differ by two hours (Table 2). The top and bottom panels of Fig. 6 show the rainfall distributions at the times of peak rainfall in the RRA data and the WRF model, respectively.

At 20 JST on 28 May, the RRA data (Fig. 6a) show a maximum rainfall of 114 mm near Mount Fuji (35.36°N, 138.73°E), the highest mountain in Japan. At the same location, the WRF model (Fig. 6b) simulates a maximum rainfall of 123 mm, which is close to the observed maximum rainfall and remains below 150 mm. Unlike Mount

Table 3 Summary of results from the modified WRF model

Figure	Case	Forecast	RRA rainfall mm/3 h	WRF rainfall mm/3 h	WRF Area $\geq$ 500 km^2	DIS km
2	1	Yes	150	144	Yes	53
	7	Yes	194	190	Yes	73
	8	Yes	260	289	No	59
3	2	Yes	146	166	Yes	31
	6	Yes	139	158	Yes	54
	9	Yes	150	170	Yes	91
4	3	Partial	240	116 (56)	No	255 (46)
	4	Partial	193	112	No	27
5	5	No	212	174	No	178
	10	No	345	339	Yes	200
6	A	Yes	114	123	No	3
		No	86	164	No	57
7	B	Yes	135	138	Yes	54
	F	Yes	134	124	No	23
8	C	Yes	99 (71)	175 (90)	Yes (No)	89 (16)
	D	Yes	80 (80)	120 (40)	Yes (No)	95 (7)
	E	Yes	98 (63)	127 (40)	Yes (No)	416 (66)

Cases are listed in the order shown in Figs. 2, 3, 4, 5, 6, 7 and 8. Forecast denotes the degree of forecast performance. For Cases 1–10, Yes, Partial, and No denote reasonable reproduction of both rainband formation and rainfall exceeding 150 mm in 3 h, reasonable reproduction of rainband formation only, and forecast failure, respectively. For Cases A–F, Yes and No denote reasonable reproduction of rainband formation with rainfall remaining below 150 mm in 3 h and forecast failure, respectively. Numbers in parentheses for Case 3 indicate the values obtained when the rainband near the Noto Peninsula is excluded, whereas those for Cases C–E indicate the values obtained when the rainbands near the typhoon eyewalls are excluded

Moriyoshi (Fig. 3b), Mount Fuji is adequately resolved at a 5-km grid spacing. Although the ORG model (Fig. 6c) also simulates rainfall near the mountain, it produces excessive rainfall over a mountain range near 36°N, 137.5°E.

At 22 JST on 28 May, the rainfall near Mount Fuji in the RRA data has almost ceased (Fig. 6d). However, rainfall near the mountain in the WRF model intensifies and exceeds 150 mm (Fig. 6e). Thus, the simulated maximum rainfall satisfies the rainfall criterion, despite the observed maximum rainfall of 114 mm at 20 JST (Fig. 6a). To avoid a false alarm when only the rainfall criterion is considered, the WRF model may require further improvement to suppress excessive rainband development. Rainfall near the mountain in the ORG model also persists but is weaker than that in the WRF model (Fig. 6f).

4.2.2 Cases B and F

Figure 7 is the same as Fig. 2, but for Cases B and F. For Case B, a low-pressure system accompanied by a front passed near Shikoku (e.g., JWA 2026). The RRA data (Fig. 7a) show a rainband with a maximum rainfall of 135 mm along the southeastern coast of Shikoku, whereas the WRF model (Fig. 7b) simulates a rainband with a maximum rainfall of 138 mm over central Shikoku. Over the ocean south of Shikoku, the WRF surface winds are more easterly than the ERA5 winds. The westward displacement of the simulated rainband is consistent with the more easterly WRF surface winds. In contrast, the ORG model (Fig. 7c) produces a maximum rainfall exceeding 150 mm.

For Case F, a typhoon moved northwestward over the ocean south of Kyushu while intensifying (e.g., JWA 2026). Both the RRA data and the WRF model (Fig. 7d and e) show a rainband on the western side of the Tokai region, with a maximum rainfall of 134 and 124 mm, respectively. In contrast, although a rainband simulated by the ORG model also remains below 150 mm (Fig. 7f), it is more intense and displaced farther to the lee side than the rainbands in both the RRA data and the WRF model.

4.2.3 Cases C, D, and E

Figure 8 is the same as Fig. 2, but for Cases C, D, and E. In these cases, the typhoon centers were located over the ocean east of Japan (e.g., JWA 2026), and the ERA5 surface winds blowing from the ocean were easterly to northeasterly (Fig. 8a and d, and 8g). The RRA data (Fig. 8a and d, and 8g) show maximum rainfall below 100 mm, with rainfall over land generally not exceeding 80 mm (Fig. 8d). Both the WRF (Fig. 8b and e, and 8h) and ORG (Fig. 8c and f, and 8i) models generally simulate rainbands in locations similar to the observed rainbands and produce rainfall below 90 mm over land. However, the simulated rainfall, likely associated with the typhoon eyewalls, is more intense than the observed rainfall. The difference in rainfall near the

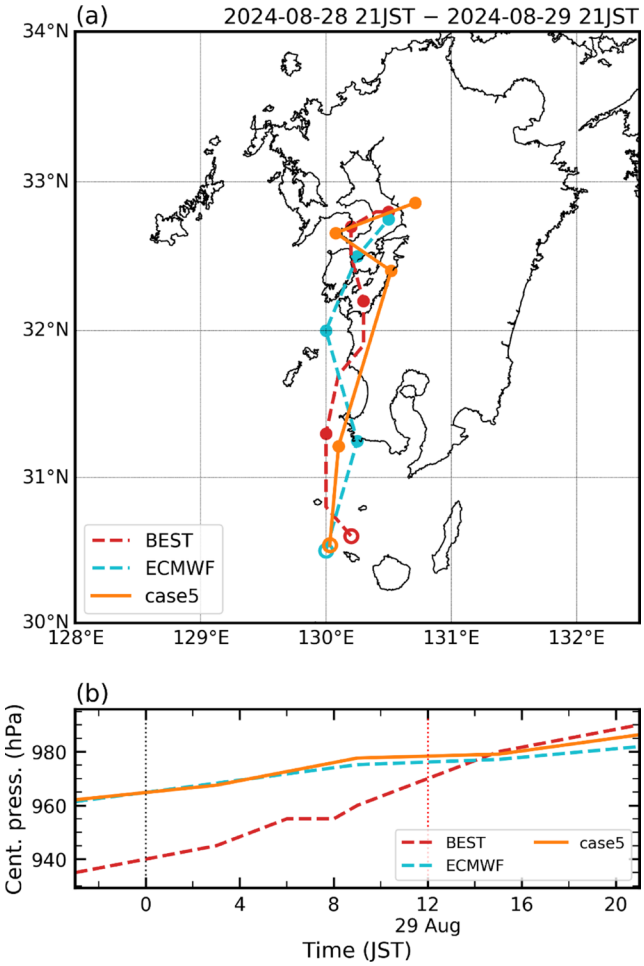


Fig. 9 (a) Typhoon track and (b) central pressure from the best-track data (red dashed line), the ECMWF data (cyan dashed line), and the modified WRF model (orange solid line). For the ECMWF data and the modified WRF model, central pressure is defined as the minimum sea level pressure. Open and filled circles in (a) indicate typhoon-center positions at the initial time and at 6-h intervals, respectively

eyewalls between the RRA data and the models is discussed in Sect. 5.

5 Discussion

Table 3 summarizes the results from the modified WRF model. The ORG model also reproduced several cases reasonably well. Nevertheless, the modified WRF model performed no worse than the ORG model in almost all cases and showed substantial improvement in several cases. In this section, we discuss the causes of the remaining issues and the challenges for further model improvement.

5.1 Forecast failure

The modified WRF model performed poorly in Cases 5 and 10 (Fig. 5). For Case 5, Fig. 9 shows the typhoon track and central pressure from the WRF model together with the best-track data provided by the Regional Specialized Meteorological Center Tokyo (JMA 2026d). Although the positions of the simulated typhoon centers at 6-h intervals (orange circles in Fig. 9a) are somewhat scattered because of the relatively flat pressure distribution around the simulated typhoon centers, they do not differ greatly from the best-track positions (red circles). In contrast, the initial central pressure of about 960 hPa from the ECMWF data is approximately 26 hPa higher than that in the best-track data (Fig. 9b). This substantial discrepancy in the initial pressure may have contributed to the poor performance of the modified WRF model. This issue cannot be resolved solely by improving subgrid-scale parameterizations and may require improvements to the initial conditions through appropriate data assimilation techniques (e.g., Xiao et al. 2006; Zhu et al. 2026). Bonavita et al. (2017) showed that modifications to the ECMWF data assimilation system improved the initial representation of tropical cyclones and the resulting analyses.

Figure 10 illustrates the horizontal distributions of surface air temperature, surface wind, and sea level pressure from the ERA5 data (ECMWF 2026b), ECMWF data, and modified WRF model for Case 10. The ERA5 data

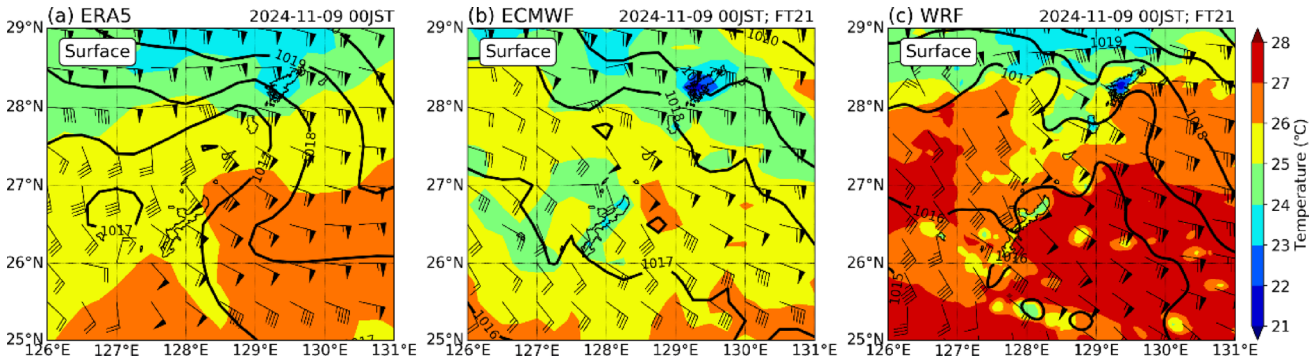


Fig. 10 Horizontal distributions of surface air temperature (shading), surface wind (barbs), and sea level pressure (contours) from (a) the ERA5 data, (b) the ECMWF data, and (c) the modified WRF model for Case 10 at the start of the 3-h accumulation period (00 JST on 09 November). A flag, full barb, and half barb denote wind speeds of 10, 2, and 1 m s^{-1}, respectively

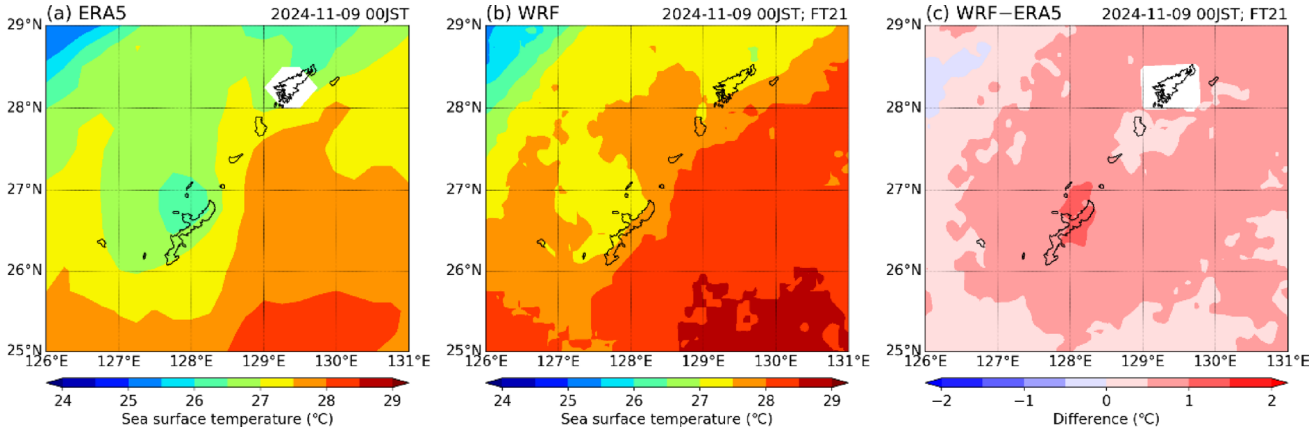


Fig. 11 Horizontal distributions of sea surface temperature from (a) the ERA5 data, (b) the modified WRF model (daily HIMSST data), and (c) their difference for Case 10 at the start of the 3-h accumulation period (00 JST on 09 November)

(Fig. 10a) show a pressure trough extending northeastward from Okinawa Island, which gradually developed after about 18 JST on 08 November (FT15). This trough may be responsible for the rainfall pattern shown in Fig. 5d. Neither the ECMWF data (Fig. 10b) nor the WRF model (Fig. 10c) reproduces such a well-defined trough. Whether data assimilation can reproduce such a pressure trough remains unclear and should be examined in future studies.

5.2 Sea surface conditions

Unrelated to the pressure trough, Fig. 10 shows that the WRF model produces surface air temperatures approximately 0–2 °C higher than those in the ERA5 data. This warm bias may be associated with differences in sea surface temperatures between the ERA5 and HIMSST datasets and/or differences in surface heat fluxes between the ERA5 data and the WRF model. Indeed, the sea surface temperature around Okinawa Island in the HIMSST data was about 0–1 °C higher than that in the ERA5 data (Fig. 11).

Similar issues for rainfall, rather than temperature, were identified in Cases C, D, and E (Fig. 8), in which the simulated rainfall near the typhoon eyewalls over the ocean was larger than that in the RRA data. Radar-based rainfall estimates generally become less accurate with increasing distance from the radar and may underestimate rainfall at long ranges (e.g., Kitchen and Jackson 1993). However, the heavy rainfall and high surface air temperatures may also be attributable to excessive surface latent and sensible heat fluxes, respectively. Reexamination of the sea surface temperature data and parameters in the surface layer scheme, such as the roughness length over water, may therefore be warranted.

5.3 Mass-flux scheme

In the current mass-flux scheme, the assumption of $w_{ui} - \overline{w} \approx w_{ui}$ was used (see Sect. 3.1). Near typhoon eyewalls, however, $\overline{w}$ may not be negligible even at a relatively coarse 5-km grid spacing. The impact of reintroducing $\overline{w}$ should be investigated.

For the nighttime events of Cases 3 and 4 (Fig. 4), the simulated rainfall was lower than both the observed rainfall and the 150-mm rainfall criterion. Under nocturnal stable conditions, the current mass-flux scheme is generally inactive. The weaker rainfall and leeward displacement of the simulated rainbands suggest that the absence of the second term on the right-hand side of Eqs. (1) and (4) may lead to inadequate simulations of rainband location and rainfall intensity. The current mass-flux scheme only considers plumes rising from the surface (see Sect. 3.2.2). In the absence of such plumes, incorporating updrafts originating from the lifting condensation level, like the shallow cumulus parameterization of Neggers et al. (2002), may improve the prediction of rainband location and rainfall intensity.

Furthermore, the modified WRF model produced excessive rainfall around Mount Fuji in Case A (Fig. 6). This event also occurred at night, and its simulation may therefore be improved by the above modification to the mass-flux scheme. As described in Sect. 3.1, the mass-flux term in Eq. (4) can become negative and moderate turbulence growth. However, whether this effect suppresses rainband development remains under investigation.

6 Conclusions

Using the modified WRF model, we conducted sixteen simulations of heavy rainfall events, including linear rainbands, to evaluate its applicability to heavy rainfall information.

The events consisted of ten missed-issuance cases and six false-alarm cases. Model results were compared with the RRA data, with a primary focus on maximum rainfall. For reference, results from the ORG model using the original mass-flux scheme were also presented. The modified WRF model performed no worse than the ORG model in almost all cases and showed substantial improvement in several cases.

For eight of the ten missed-issuance cases, the WRF model reasonably simulated the occurrence of heavy rainfall (Figs. 2, 3 and 4). The distance between the rainfall maxima in the RRA data and the WRF model (DIS) was approximately 54 km on average, which tended to be relatively large for frontal rainfall (e.g., Figs. 2e and 3h) but relatively small for orographic rainfall (e.g., Fig. 4e). In two of these eight cases, both of which occurred inland at night, the WRF model underestimated rainfall intensity (Fig. 4). Furthermore, the WRF model performed poorly in the remaining two cases, which occurred within the influence of a typhoon or over the ocean on the southern periphery of a high-pressure system (Fig. 5).

For five of the six false-alarm cases, the WRF model reasonably reproduced the observed rainfall that did not satisfy the linear-rainband criteria (Figs. 7 and 8). However, rainfall near typhoon eyewalls over the ocean may be overestimated. In contrast, for the remaining event, the WRF model simulated heavy rainfall exceeding the 150-mm rainfall criterion near Mount Fuji (Fig. 6), the cause of which remains under investigation.

Further evaluation using a larger number of rainfall events, including cases with correct FILR decisions, is needed. Nevertheless, this study suggests that the modified WRF model has the potential to complement JMA FILR decisions and contribute to reducing both missed issuances and false alarms. We currently perform real-time forecasts every 6 h. Based on the present results, forecasts with lead times of 17–25 h may be suitable for supporting FILR decisions, as they are available approximately half a day before the expected rainband formation.

However, several challenges remain, including poor performance within typhoon-affected regions, possible overestimation of sea surface temperature and surface heat fluxes over the ocean, and the underestimation of rainfall during nighttime events. Future work to address these challenges includes:

- Introducing data assimilation techniques into the model,
- Reexamining the sea surface temperature data and parameters in the surface layer scheme, such as the roughness length over water, and.
- Reintroducing $\overline{w}$ and incorporating updrafts originating from the lifting condensation level into the mass-flux scheme.

Supplementary Information The online version contains supplementary material available at https://doi.org/10.1007/s44394-026-00041-4.

Acknowledgements The first author would like to thank the management at the Japan Weather Association for giving him the opportunity to improve the WRF model. The authors thank two anonymous reviewers for their valuable suggestions for improving the manuscript.

Author contributions M.N. conceived the study, developed the model, performed the simulations and analyses, and wrote the manuscript. Y.Y. reviewed the manuscript.

Data availability The WRF model was downloaded from https://www2.mmm.ucar.edu/wrf/users/. The WRF-Python graphical software was downloaded from https://wrf-python.readthedocs.io/en/latest/. The operational forecast data was purchased from the ECMWF. The HIMSST data was downloaded from https://ds.data.jma.go.jp/gmd/goos/data/rrtdb/jma-pro.html. The best track data was downloaded from https://www.jma.go.jp/jma/jma-eng/jma-center/rsmc-hp-pub-eg/besttrack.html. The ERA5 reanalysis data was downloaded from https://cds.climate.copernicus.eu/datasets.

Declarations

Conflict of interest The authors declare no competing interests.

Open Access This article is licensed under a Creative Commons Attribution 4.0 International License, which permits use, sharing, adaptation, distribution and reproduction in any medium or format, as long as you give appropriate credit to the original author(s) and the source, provide a link to the Creative Commons licence, and indicate if changes were made. The images or other third party material in this article are included in the article's Creative Commons licence, unless indicated otherwise in a credit line to the material. If material is not included in the article's Creative Commons licence and your intended use is not permitted by statutory regulation or exceeds the permitted use, you will need to obtain permission directly from the copyright holder. To view a copy of this licence, visit http://creativecommons.org/licenses/by/4.0/.

References

Bonavita M, Dahoui M, Lopez P, Prates F, Hólm E, De Chiara G, Geer A, Isaksen L, Ingleby B (2017) On the initialization of tropical cyclones. ECMWF Tech Memoranda 810. https://doi.org/10.21957/insgrw8u6

ECMWF (2026a) IFS Medium-range Control forecast (formerly HRES) and Analysis Data (15-days) (Set I). https://www.ecmwf.int/en/forecasts/datasets/set-i. Accessed 1 March 2026

ECMWF (2026b) ERA5 hourly data on single levels from 1940 to present. https://cds.climate.copernicus.eu/datasets. Accessed 1 March 2026

JWA (2026) Past weather chart (in Japanese). https://tenki.jp/past/chart/. Accessed 1 March 2026

JMA (2026a) FY 2024: Forecast information on linear rainbands and actual conditions (in Japanese). https://www.jma.go.jp/jma/kisho

u/know/jirei/jirei_senjoukousuitai_2024.html. Accessed 1 March 2026

JMA (2026b) Forecasting technology for linear rainbands is advancing (in Japanese). https://www.jma.go.jp/jma/press/2603/13a/20260313_nwp.html. Accessed 1 July 2026

JMA (2026c) NEAR-GOOS Regional Real Time Data Base. https://ds.data.jma.go.jp/gmd/goos/data/rrtdb/jma-pro.html. Accessed 1 March 2026

JMA (2026d) RSMC Best Track Data (Text). https://www.jma.go.jp/jma/jma-eng/jma-center/rsmc-hp-pub-eg/besttrack.html. Accessed 1 March 2026

Kato T (2020) Quasi-stationary band-shaped precipitation systems, named Senjo-Kousuitai, causing localized heavy rainfall in Japan. J Meteorol Soc Jpn 98:485–509. https://doi.org/10.2151/jmsj.2020-029

Kato T, Goda H (2001) Formation and maintenance processes of a stationary band-shaped heavy rainfall observed in Niigata on 4 August 1998. J Meteorol Soc Jpn 79:899–924. https://doi.org/10.2151/jmsj.79.899

Kato R, Shimizu S, Shimose K, Hirano K, Shiraishi K, Yoshida S, Sakai T, Nagai T (2024) Improvement of two-hour-ahead QPF using blending technique with spatial maximum filter for tolerating forecast displacement errors and water vapor lidar assimilation. J Meteorol Soc Jpn 102:445–464. https://doi.org/10.2151/jmsj.2024-024

Kawabata T, Kuroda T, Seko H, Saito K (2011) A cloud-resolving 4DVAR assimilation experiment for a local heavy rainfall event in the Tokyo metropolitan area. Mon Wea Rev 139:1911–1931. https://doi.org/10.1175/2011MWR3428.1

Kawano T, Kawamura R (2020) Genesis and maintenance processes of a quasi-stationary convective band that produced record-breaking precipitation in northern Kyushu, Japan on 5 July 2017. J Meteorol Soc Jpn 98:673–690. https://doi.org/10.2151/jmsj.2020-033

Kitchen M, Jackson PM (1993) Weather radar performance at long range—Simulated and observed. J Appl Meteorol 32:975–985. https://doi.org/10.1175/1520-0450(1993)032%3C0975:WRPALR%3E2.0.CO;2

Köhler M, Ahlgrimm M, Beljaars A (2011) Unified treatment of dry convective and stratocumulus-topped boundary layers in the ECMWF model. Quart J Roy Meteorol Soc 137:43–57. https://doi.org/10.1002/qj.713

Nagata K (2011) Quantitative precipitation estimation and quantitative precipitation forecasting by the Japan Meteorological Agency. RSMC Tokyo Typhoon Cent Tech Rev 13:37–50. https://www.jma.go.jp/jma/jma-eng/jma-center/rsmc-hp-pub-eg/techrev/text13-2.pdf Accessed 1 March 2026

Nakanishi M (2023) Reevaluating the surface energy balance and soil thermal diffusion equations in the Noah multi-parameterization (Noah-MP) scheme. https://doi.org/10.2151/sola.2023-018. SOLA 19:135 – 141

Nakanishi M (2024) Contribution of shallow convection to the localization of a band-shaped area of heavy precipitation on 4 July 2020. SOLA 20:1–7. https://doi.org/10.2151/sola.2024-001

Nakanishi M (2025) A modified parameterization of the buoyancy production of turbulent kinetic energy to improve the transition to deep convection. SOLA 21:9–16. https://doi.org/10.2151/sola.2025-002

Nakanishi M, Niino H (2009) Development of an improved turbulence closure model for the atmospheric boundary layer. J Meteorol Soc Jpn 87:895–912. https://doi.org/10.2151/jmsj.87.895

Neggers RAJ (2015) Exploring bin-macrophysics models for moist convective transport and clouds. J Adv Model Earth Syst 7:2079–2104. https://doi.org/10.1002/2015MS000502

Neggers RAJ, Siebesma AP, Jonker HJJ (2002) A multiparcel model for shallow cumulus convection. J Atmos Sci 97:1655–1668. https://doi.org/10.1175/1520-0469(2002)059%3C1655:AMMFSC%3E2.0.CO;2

Oizumi T, Saito K, Ito J, Kuroda T, Duc L (2018) Ultra-high-resolution numerical weather prediction with a large domain using the K computer: A case study of the Izu Oshima heavy rainfall event on October 15–16, 2013. J Meteorol Soc Jpn 96:25–54. https://doi.org/10.2151/jmsj.2018-006

Olson JB, Kenyon JS, Angevine WA, Brown JM, Pagowski M, Sušelj K (2019) A description of the MYNN-EDMF scheme and the coupling to other components in WRF–ARW. https://doi.org/10.25923/n9wm-be49. NOAA Technical Memorandum OAR GSD-61

Ono K, Ito J (2024) Numerical simulation of a case of heavy rainfall in the northern Tohoku region of Japan on 9 August 2013. https://doi.org/10.2151/sola.20A-001. SOLA 20A:1 – 9

Ota T, Igarashi Y (2026) Impact-based forecasting in Japan: a review of the Japan meteorological agency's real-time risk map Kikikuru. J Meteorol Soc Jpn 104:32. https://doi.org/10.1007/s44394-026-00034-3

Siebesma AP, Cuijpers JWM (1995) Evaluation of parametric assumptions for shallow cumulus convection. J Atmos Sci 52:650–666. https://doi.org/10.1175/1520-0469(1995)052%3C0650:EOPAFS%3E2.0.CO;2

Skamarock WC, Klemp JB, Dudhia J, Gill DO, Liu Z, Berner J, Wang W, Powers JG, Duda MG, Barker DM, Huang X-Y (2019) A description of the Advanced Research WRF Version 4. NCAR Tech Note NCAR/TN-556 + STR. https://doi.org/10.5065/1dfh-6p97

Sušelj K, Teixeira J, Chung D (2013) A unified model for moist convective boundary layers based on a stochastic eddy-diffusivity/mass-flux parameterization. J Atmos Sci 70:1929–1953. https://doi.org/10.1175/JAS-D-12-0106.1

Tochimoto E, Iizuka S, Ohigashi T (2022) Influence of an upper-level trough on the formation of a Baiu frontal depression that caused a torrential rainfall event in southern Kyushu, Japan on July 4, 2020. https://doi.org/10.2151/sola.18A-001. SOLA 18A:1 – 7

Xiao Q, Kuo YH, Zhang Y, Barker DM, Won DJ (2006) A tropical cyclone bogus data assimilation scheme in the MM5 3D-Var system and numerical experiments with Typhoon Rusa (2002) near landfall. J Meteorol Soc Jpn 84:671–689. https://doi.org/10.2151/jmsj.84.671

Zhu K, Zhao D, Xu X, Sun S, Shi W (2026) Toward improved tropical cyclone forecasting: An optimized strategy combining dynamic initialization and bogus data assimilation. J Geophys Res: Atmos 131. https://doi.org/10.1029/2026JD046976. e2026JD046976

Publisher's note Springer Nature remains neutral with regard to jurisdictional claims in published maps and institutional affiliations.